# Importance of van der Waals interactions and cation-anion coupling in an organic quantum spin liquid

P. Lazić,[1] M. Pinterić,[2,3] D. Rivas Góngora,[2] A. Pustogow,[4] K. Treptow,[4] T. Ivek,[2] O. Milat,[2] B. Gumhalter,[2] N. Došlić,[1] M. Dressel,[4] and S. Tomić[2,*]

[1]*Rudjer Bošković Institute, Bijenička Cesta 54, HR-10000 Zagreb, Croatia*
[2]*Institut za fiziku, Bijenička cesta 46, HR-10000 Zagreb, Croatia*
[3]*Faculty of Civil Engineering, Smetanova 17, SI-2000 Maribor, Slovenia*
[4]*1. Physikalisches Institut, Universität Stuttgart, D-70550 Stuttgart, Germany*

The Mott insulator $\beta'$-EtMe$_3$Sb[Pd(dmit)$_2$]$_2$ belongs to a class of charge transfer solids with highly frustrated triangular lattice of $S = 1/2$ molecular dimers and a quantum-spin-liquid ground state. Our experimental and *ab initio* theoretical studies show the fingerprints of strong correlations and disorder, the important role of cation-dimer bonding in charge redistribution, no sign of intra- and interdimer dipoles, and the decisive van der Waals contribution to interdimer interactions and the ground-state structure. The latter consists of quasidegenerate electronic states related to the different configurations of cation moieties, which permit two different equally probable orientations. Upon reducing the temperature, the low-energy excitations slow down, indicating glassy signatures as the cation motion freezes out.

## I. INTRODUCTION

Quantum spin liquid (QSL), a highly correlated fluctuating quantum spin state, is a long-standing intriguing phenomenon in physics [1,2]. It is expected to appear in geometrically frustrated systems when strong quantum fluctuations suppress the long-range magnetic order. Recently, the QSL has been realized in materials with frustrated lattices at the insulating side of Mott transition [3]. Because of this exciting discovery, considerable efforts have been devoted to the studies of organic Mott insulators—charge transfer crystalline solids in which electrons are strongly correlated and confined to two dimensions. They form layers with triangular structures of molecular pairs–dimers with an odd number of electrons separated by nonconducting inorganic moities.

Three organic Mott systems with different degrees of correlations [4] $\kappa$-(BEDT $-$ TTF)$_2$Cu$_2$(CN)$_3$ (short $\kappa$-CuCN), $\kappa$-(BEDT $-$ TTF)$_2$Ag$_2$(CN)$_3$ (short $\kappa$-AgCN), and $\beta'$-EtMe$_3$Sb[Pd(dmit)$_2$]$_2$ (short $\beta'$-EtMe$_3$Sb) exhibit an anomalous electrodynamic response below 60 K [4–8], while at very low temperatures the magnetic and thermodynamic response exhibits unconventional behavior ascribed to the QSL ground state [9–11]. The full understanding of the nature of QSL is missing primarily because frustrated triangular lattices on their own are unable to destroy the long-range magnetic order [12]. It was suggested that an additional, exotic spin-dipolar coupling in the presence of geometrical frustration would suffice to induce quantum fluctuations and suppress magnetic ordering, however its experimental confirmation is still lacking [13–17]. The mechanism of dipolar-spin coupling relies on the Coulomb interactions

within the sublattice of molecular dimers only, thereby completely neglecting the role of inorganic moieties to which the molecular sublattice is strongly hydrogen-bonded. For $\kappa$-CuCN and $\kappa$-AgCN, the decisive role of cation-anion hydrogen bonding is revealed by the experimental results combined with *ab initio* numerical calculations. This points to a significant anion-driven renormalization of the electronic properties due to disorder by cyanide isomorphism [7,8]. Notably, despite the fact that single crystals of these two BEDT-TTF materials are nominally pure, the variable-range hopping, relaxor dielectric response, and anomalous terahertz response are observed within the molecular planes as a result of the entangled charge and lattice excitations.

An important question thus arises on the role of random disorder in QSL formation. Does it only modify the QSL and make the interpretation of experiments more difficult, or is it inherently related to the establishment of QSL [18]? To shed more light on the mechanism of QSL entanglement in organic Mott insulators, and having in mind the proposed role of dipolar-spin coupling, we have investigated the QSL organic material $\beta'$-EtMe$_3$Sb that consists of different molecular pairs and nonconducting ionic moieties [Fig. 1(a)] [19]. Evidence for QSL is provided by the susceptibility and nuclear magnetic resonance measurements, which show no sign of classical phase transition down to 30 mK but indicate the presence of an effective antiferromagnetic exchange interaction of the order of 250 K [11]. In this paper, we advance the understanding of this QSL Mott insulator by our results of dc transport, low-frequency dielectric and vibrational spectroscopy (see Appendix A), and supporting density-functional theory (DFT) calculations. This allows us to unambiguously identify the origin of anomalous charge response in the cation disorder and motion mapped by hydrogen bonding onto the molecular dimers. We find that the ground state consists of quasidegenerate
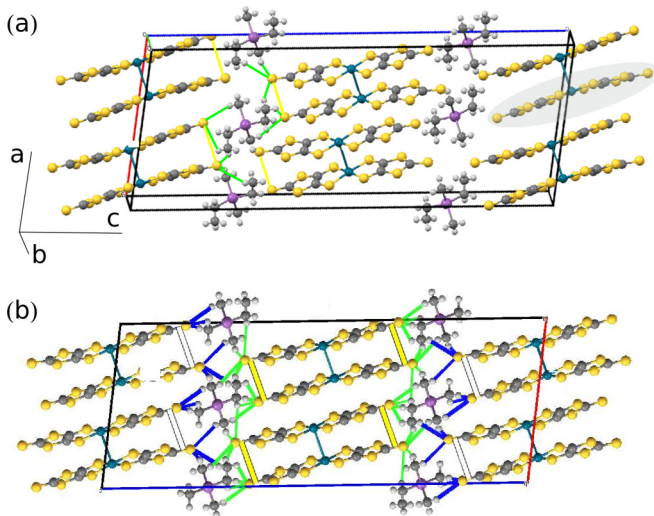
FIG. 1. (a) Side view of extended unit cell in $C2/c$ symmetry of $\beta'$-EtMe$_3$Sb. The molecule Pd(dmit)$_2$ is shown within the shaded area. Yellow, grey, green, light grey, and violet circles denote sulfur, carbon, palladium, hydrogen, and antimony atoms, respectively. H-bonds between the terminal S atoms of Pd(dmit)$_2$ molecules and H of Et (CH$_2$-CH$_3$) or Me (CH$_3$) groups of cations are marked by green lines. (b) Relaxed ground-state structure in the $ac$ plane projected along the $b$ axis as obtained from DFT calculations. Et and the Me sites are in the proximity of S atoms of dimers in the central and side layer, respectively. There are eight short contacts (green lines) between two S atoms at one end of the dimer and cations in the central layer, while there are only six contacts (blue lines) in the side layer. Yellow and white lines denote large and small S-S dimer openings near the Et and Me groups, respectively.
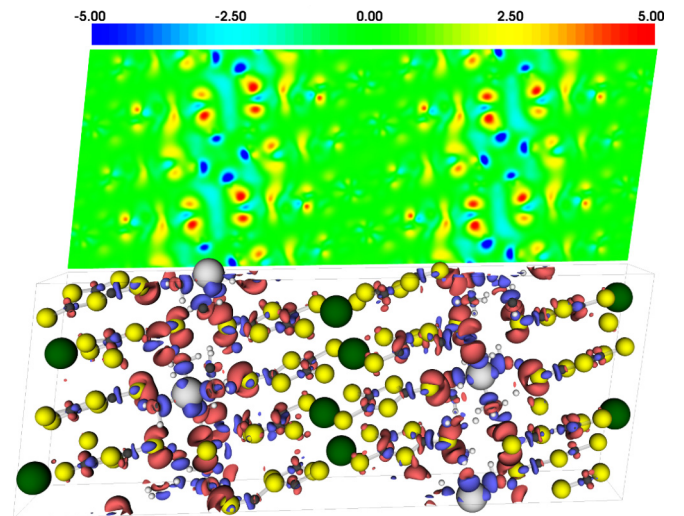


FIG. 2. Lower panel: Cation-anion interaction-induced electronic charge redistribution in the relaxed ground state calculated as the difference between the charge density of the complete system and its constituents, i.e., cations and anions. Two isosurfaces are shown: electron accumulation (red) and depletion (blue). Balls of different color denote different atoms in the structure. The largest electron accumulation is concentrated close to the end S sites of [Pd(dmit)$_2$]$_2$ dimers; it is much more enhanced near Et than Me sites. Upper panel: the averaged charge density in the $ac$ plane (see Appendix C). The color bar shows charge transfer ($e/\text{Å}^2$).

electronic states with reduced symmetry, the formation of which is most appropriately considered as a cooperative effect of the EtMe$_3$Sb cation - [Pd(dmit)$_2$]$_2$ anion coupling. This reveals that the effective interdimer interaction results from the interplay between attractive van der Waals interactions and Pauli repulsion.

## II. SIGNATURES OF VAN DER WAALS INTERACTIONS IN THE ELECTRONIC STRUCTURE

Randomness in $\beta'$-EtMe$_3$Sb is revealed by x-ray diffraction measurements [20]. These data show that Et groups of four cations in the unit cell occupy one of the two different equally probable orientations [Fig. 1(a)], indicating that the formation of several crystallographic configurations is possible (see Appendix B). To get an insight as to how the randomness affects the electronic properties of $\beta'$-EtMe$_3$Sb, we have performed DFT calculations by using the self-consistently implemented nonlocal van der Waals density functional (vdW-DF) [21–23] for correlation and optB88 for exchange [24]. In that sense, our approach differs from the DFT calculations applied previously [25–28]. The entire $\beta'$-EtMe$_3$Sb system, with atomic positions and unit cell parameters, relaxes into a structure of minimum energy when both ends of molecular dimers in each of the two layers in the unit cell are in the same cation environment. The space group of the relaxed ground-state structure is reduced to P$\bar{1}$. In the center and side layer, the dimer ends are next

to the Et and Me groups, respectively [Figs. 1(b) and 2, lower panel]. Here it is worth noting that DFT relaxation without vdW interaction yields a structure with a 22% larger unit cell than found experimentally, whereas the vdW-DF relaxed structure meets the experimental one to within 4%. The inadequacy of DFT calculations without the vdW interactions is especially striking in the dimer plane: the $a$ and $b$ unit cell parameters are enlarged by almost 10% (see Appendix C), thus indicating the significant role of nonlocal vdW binding contribution to the effective interdimer interactions within the $ab$ plane, as well as to the total cohesion energy of $\beta'$-EtMe$_3$Sb crystal. This failure of the semilocal DFT was less apparent in the $\kappa$-CuCN and $\kappa$-AgCN, where the calculated structure deviated by 10% and 14% from the experimental one, respectively [29]. Furthermore, we analyze the bonding of the system through charge rearrangement between its components. We find the largest electron accumulation in [Pd(dmit)$_2$]$_2$ dimers concentrated at the terminal S sites where chemical binding dominates. Also, it is much more enhanced near Et sites than near Me sites (Fig. 2). Accordingly, dimers establish stronger bonding with cations in Et environment than they do near Me groups. While all the contacts are shorter than the sum of van der Waals radii, the bonds are larger in number and shorter in length for Et than for the Me case [Fig. 1(b)].

The electronic band structure for the relaxed state with minimum energy is shown in Fig. 3. Globally, and apart from fine details near the Fermi energy ($E_F$), it resembles the bands obtained in previous calculations using the standard density functionals and fixed crystallographic parameters [25–28]. While due to omission of appropriate electronic correlations, all the band calculations find a half-filled band straddling
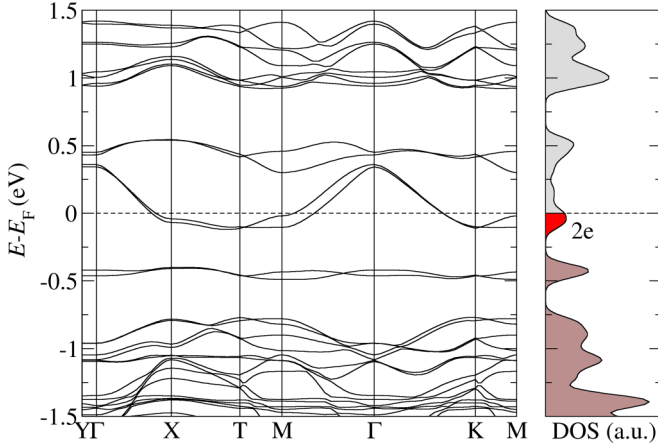
FIG. 3. Calculated band structure in the relaxed ground state of $\beta'$-EtMe$_3$Sb plotted along the high-symmetry directions. The segments $\Gamma X$, $\Gamma K$, and $\Gamma Y$ in the first Brillouin zone correspond to the $a$, $b$, and $c$ directions, respectively. Weakly dispersive bands are identified at about 0.5 eV, $-0.4$ eV, and $-1.1$ eV, while strongly dispersive bands cross the Fermi level and accommodate two electrons (red shaded area in the density of states).



FIG. 4. DC resistivity of $\beta'$-EtMe$_3$Sb versus inverse temperature indicating nearest-neighbor hopping at higher temperatures. Inset displays normalized dc conductivity within dimer planes as a function of $T^{-1/2}$, demonstrating the Efros-Shklovskii hopping due to strong electron correlations for $T \lesssim 100$ K. Data for **E** $\parallel$ $b$ are upshifted for clarity.

$E_\mathrm{F}$, the angle-resolved photoemission measurements identify the lower Hubbard band near $E_\mathrm{F}$, and a soft Mott gap [30]. In addition to strongly dispersive bands crossing $E_\mathrm{F}$, we point out two nondispersive bands, which are situated at the energies around $-0.4$ and $-1$ eV and corresponding closely to the bands observed in ARPES along the $\Gamma X$ segment. Moreover, the overall band structure around $E_\mathrm{F}$ is dominantly anion-derived. This is suggested by the result for the band structure of an isolated self-standing anion subsystem, which is only rigidly upshifted in energy if compared to the band structure of the whole anion-cation system. Finally, we find that the band structure remains almost unchanged under pressure, confirming the pertinent role of vdW forces (see Appendix C).

In addition to the relaxed state with minimum energy, we identify a manifold of electronic states in the energy range between 28 meV and 146 meV above the ground state. Remarkably, the two lowest energy states are associated with the configurations of $P\bar{1}$ and $P1$ symmetry, respectively, in which the two sides of dimers in each layer are in the same cation environment (either Et or Me), whereas their environment alternates in the central and side layers. The band structures of these quasidegenerate configurations are very similar. Conversely, the states with highest energy are associated with configurations of $C_c$ symmetry in which the two sides of dimers are in alternate cation environment, while the environment in two layers is the same. Between these two extremes, we find the states with energies ranging from 45 to 80 meV with the symmetry $P2_1/n$. Such a strong dependence on the environment can be recognized as a result of competition between attractive vdW and Pauli repulsive contributions to the interdimer interaction within the $ab$ planes. The ground-state configuration reflects the dominance of vdW interaction over Pauli repulsion whereas the reverse holds true for less probable configurations of higher energy. Importantly, the quasidegenerate electronic ground state identified by the
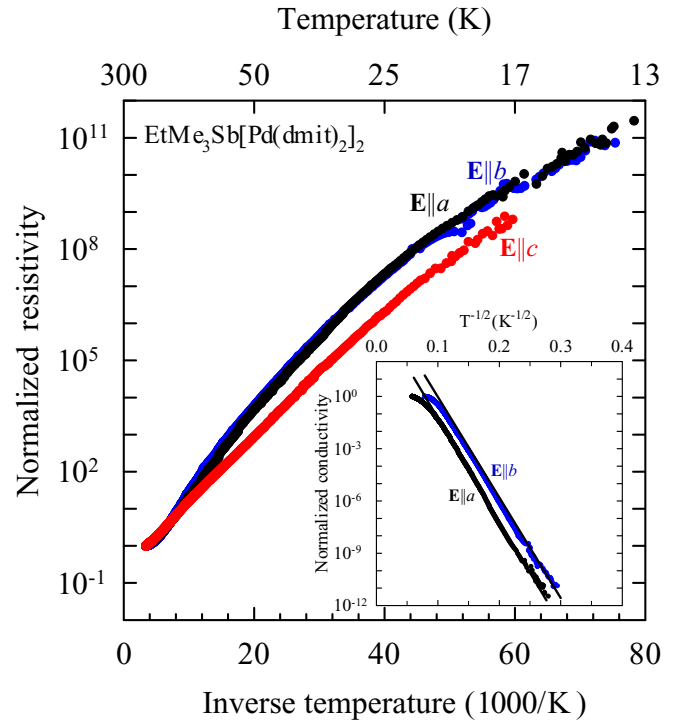
calculations implies a random domain structure in $\beta'$-EtMe$_3$Sb that is qualitatively similar to $\kappa$-CuCN and $\kappa$-AgCN [7,8].

## III. ELECTRODYNAMIC PROPERTIES

In the following, we measure the electronic properties and compare them with results of *ab initio* calculations. To this end, we explore long-wavelength charge excitations by dielectric and dc-transport measurements performed along the three crystallographic axes. We first examine the dc transport and find fingerprints of randomness and strong correlations in accord with the results of DFT calculations (Fig. 4). Especially, within the planes and at temperatures below $\sim 100$ K the hopping follows the Efros-Shklovskii temperature dependence $\sigma(T) \propto \exp[-(T_0/T)^{1/2}]$. In accord with ARPES [30], this result indicates a soft gap due to strong Coulomb interaction in disordered $\beta'$-EtMe$_3$Sb [31]. Here the electronic correlations are significantly stronger than in $\kappa$-CuCN and $\kappa$-AgCN as indicated by the optical data [4]. The effective Coulomb interaction is comparable to intradimer coupling [32]; accordingly, the gap in the calculated generic anion bands (see Appendix C) exceeds the values for $\kappa$-CuCN and $\kappa$-AgCN [7,8].

Next we focus on the dielectric function extracted from the complex conductance measured as a function of temperature (300 K–4.2 K) and frequency (40 Hz–10 MHz) (see Appendix D) [7,8]. On cooling, the real part of the dielectric function $\varepsilon'$ exhibits the relaxor-like ferroelectric behavior along the $a$ and $b$ axes within the dimer planes, as well as along the
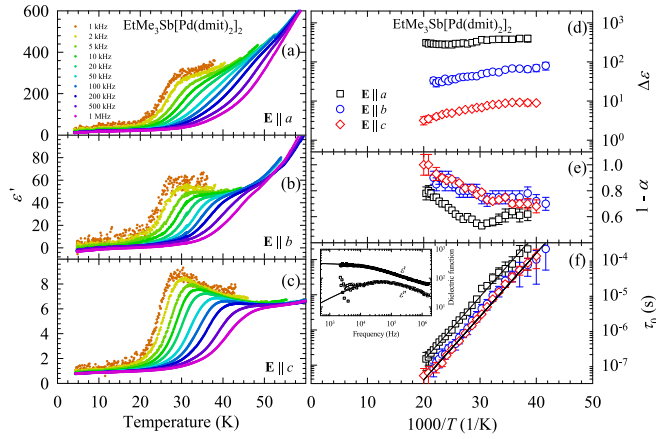
FIG. 5. (a), (b), (c) Real part of the dielectric function $\varepsilon'$ of $\beta'$-EtMe$_3$Sb versus temperature demonstrates the relaxorlike ferroelectric behavior for ac electric field applied within ($\mathbf{E} \parallel a$, $\mathbf{E} \parallel b$) and perpendicular ($\mathbf{E} \parallel c$) to the dimers plane. Dielectric strength $\Delta\varepsilon$ (d), relaxation time distribution ($1-\alpha$) (e), mean relaxation time $\tau_0$ (f) as function of inverse temperature. Inset in (f) shows double logarithmic plot of frequency dependence of real $\varepsilon'$ and imaginary $\varepsilon''$ parts of dielectric function for $\mathbf{E} \parallel a$ at 36 K. Full lines are fits to generalized Debye function $\varepsilon(\omega) - \varepsilon_{HF} = \Delta\varepsilon/[1 + (i\omega\tau_0)^{1-\alpha}]$, $\varepsilon_{HF}$ is high-frequency dielectric constant. Full lines in (f) show the Arrhenius slowing down of $\tau_0$ at the rate of 36 meV along all three crystallographic axes.

perpendicular $c$ axis (Fig. 5) [5]. $\varepsilon'$ decays down to $\sim 50\,\mathrm{K}$ where the frequency dispersion starts to develop a peak which for the lowest frequencies is situated at $\sim 25\,\mathrm{K}$. The approach based on simultaneous fits of $\varepsilon'$ and imaginary part $\varepsilon''$ of $\varepsilon(\omega)$ to the generalized Debye form reveals additional fingerprints of relaxors: a broad spectrum whose width $1-\alpha$ increases upon cooling and a gradual Arrhenius-like slowing down of the relaxation time $\tau_0$ (Fig. 5). Interestingly, the activation energy is similar along all three crystallographic axes and comparable with dc resistivity, indicating the dominant free-carrier screening. Extrapolation to 100 s gives the glass transition around 14 K.

The relaxor response suggests the existence of domains of low symmetry in accord with the DFT calculations. It allows two mechanisms of dielectric response either due to the thermally activated reorientation of dipole moments within the domains or the collective motion of interphase boundaries. The latter was recently proposed to explain anomalous dielectric response in kHz range in molecular solids [33]. Similar slow spin dynamics is present in QSL materials with disorder, its origin being unresolved [9,11,34]. To test if the dipoles emerge upon cooling in $\beta'$-EtMe$_3$Sb, we employed vibrational spectroscopy to probe the most charge-sensitive intramolecular $\nu_2$ and dimeric $\nu_1$ vibrations (see Appendix E) [35]. The data in Fig. 6(a) show no appreciable change besides the common thermal dependence. Most importantly, no splitting of either mode occurs down to 5 K, ruling out the formation of molecular and dimeric dipoles and allowing only for charge fluctuations, which are reduced when the temperature is lowered, likewise in $\kappa$-CuCN [17]. Upon cooling, the mode shows first the commonly observed hardening, whereas below 160 K it displays a redshift getting steeper under 50 K,
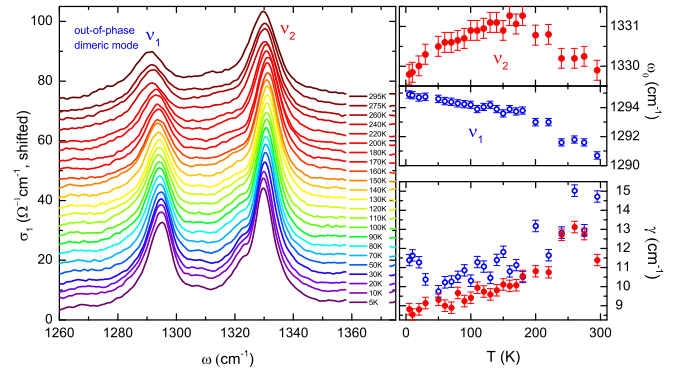


FIG. 6. Left panel: Temperature evolution of the dimeric $\nu_1$ and intramolecular vibration $\nu_2$ of $\beta'$-EtMe$_3$Sb measured for $\mathbf{E} \parallel c$. Except the 5 K data, all curves are upshifted vertically for clarity. No splitting of the mode occurs. Temperature dependence of the resonance frequency (upper right panel) and damping (lower right panel) obtained by Fano function fits of the modes.

right where the dielectric peak emerges. The cation motion below 100 K consists of internal rotations of Me groups which freeze around 40 K [34,36]. DFT calculations of the potential energy profile for Me rotation give the energy barrier of 60 meV and the first excited vibrational state only 11 meV above the ground state (see Appendix F). Thus, as the temperature lowers, this motion is gradually hindered and mapped via anion-cation coupling onto the conducting anions as a kind of dynamic disorder. Its influence is expected mostly along the $c$ axis where the layers of organic dimers and cations alternate. Indeed, the out-of-plane relaxor response is also observed in $\beta'$-[Pd(dmit)$_2$]$_2$ systems where cation disorder due to random orientation of Et groups is absent [5].

## IV. CONCLUSIONS

In conclusion, we have demonstrated a remarkable impact of both the cation-anion coupling and van der Waals interaction on the electronic properties of QSL $\beta'$-EtMe$_3$Sb[Pd(dmit)$_2$]$_2$. The disorder in nonconducting cations is identified as due to two equally probable orientations of Et groups (static disorder) and to internal rotational degrees of freedom of Me groups (dynamic). It is mapped onto the organic dimers and results in hopping dc transport and relaxor dielectric response. No sign of intra- and interdimer dipoles is observed, suggesting that low-lying excitations are due to the motion of charged domain walls. The ground state consists of quasidegenerate electronic states with reduced symmetry in which the long-range vdW force prevails over the short range Pauli repulsion. Strong correlations and vdW interactions distinguish $\beta'$-EtMe$_3$Sb from $\kappa$-CuCN and $\kappa$-AgCN. Most importantly, these three organic salts display simultaneously geometrical frustration in both organic dimers, due to the triangular structures and in the nonconducting ions. In the absence of the latter, QSL is replaced by antiferromagnetic ground state, while the relaxor peak is still observed. Hence, the disorder appears critical for the prevalence of QSL over the antiferromagnetic ordering. We expect that the present paper will stimulate further studies of the microscopic understanding of this phenomenon.

## APPENDIX A: EXPERIMENTAL DETAILS

High-quality single crystals of $\beta'$-EtMe$_3$Sb[Pd(dmit)$_2$]$_2$ (short $\beta'$-EtMe$_3$Sb) grown at RIKEN, Japan [19,20] were investigated in the temperature range between 300 K and 4.2 K. Dielectric spectroscopy and dc-transport measurements were carried out along the $a$ and $b$ axes within and the $c$ axis perpendicular to the molecular planes. The typical crystal dimensions were $1 \times 0.3 \times 0.05$ mm$^3$. Electrical contacts were prepared parallel to the sample edges so as to enable the measurements along one of the three crystallographic directions. We have also performed measurements on differently shaped samples ($0.4 \times 0.3 \times 0.05$ mm$^3$) along the in-plane axes cut from a single crystal oriented by recording the midinfrared spectra.
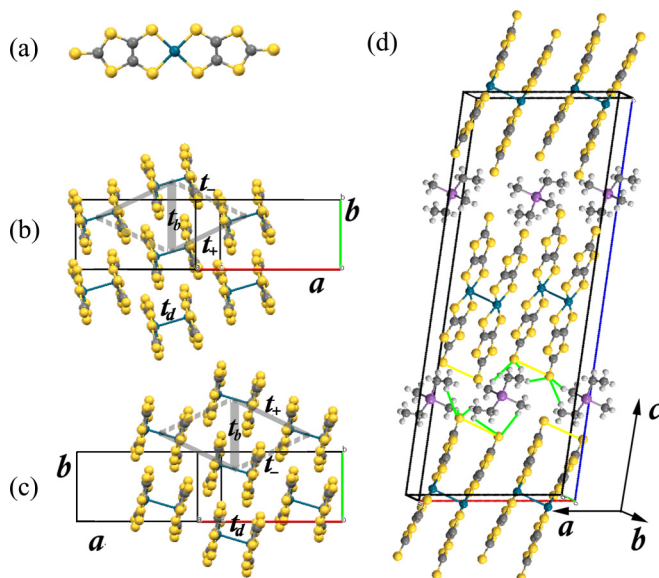


FIG. 7. (a) Sketch of the molecule Pd(dmit)$_2$, where dmit = 1,3-dithiole-2-thione-4,5-dithiolate: yellow, grey, and green circles denote sulfur, carbon, and palladium atoms, respectively. (b), (c) View of Pd(dmit)$_2$ dimers in the $ab$ plane projected along the direction tilted 17° away from the $c$ axis. (b) and (c) panels show dimers in two neighboring layers which have different stacking directions ($a + b$) and ($a - b$), respectively. An almost isotropic triangular lattice is denoted by gray lines, the interdimer transfer integrals are labeled by $t_b$ (thick gray), and $t_+$ (thin gray), and $t_-$ (dashed gray), while the intradimer transfer integral is labeled by $t_d$. (d) Side view of extended unit cell in $C2/c$ symmetry. Light grey and violet circles denote hydrogen and antimony atoms, respectively. Possible hydrogen bonds between the end S ions of the Pd(dmit)$_2$ molecules and H of Et (CH$_2$-CH$_3$) or Me (CH$_3$) groups of the cations are indicated by full green lines.
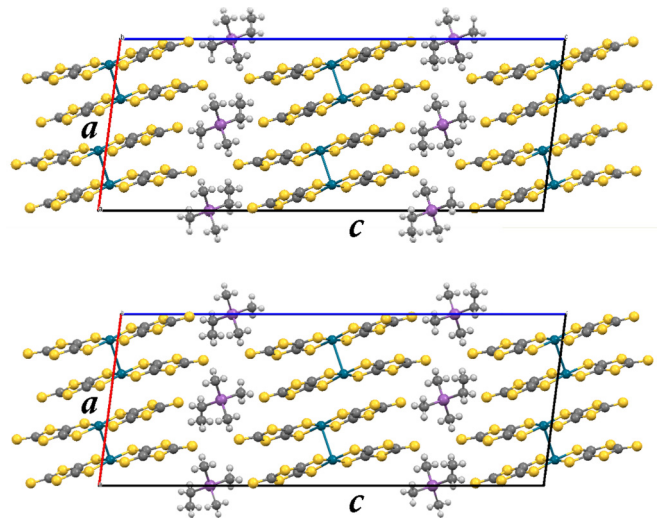


FIG. 8. Two relaxed configurations of $\beta'$-EtMe$_3$Sb, the state with minimum energy (upper panel) and the state with energy higher by 28 meV (lower panel) in the $ac$ plane projected along the $b$ axis. In both configurations, two ends of each dimer are in same environment, while the environment is different in the center and side layer. In the former configuration, the dimer ends are near to Et in the center layer, while they are near to the Me groups in the side layer. It is just the opposite in the latter, i.e., dimers' ends are near Me in the center layer, while they are near Et groups in the side layer. Yellow, grey, light grey, and violet circles denote sulfur, carbon, hydrogen, and antimony atoms, respectively. The unit cell is marked as a parallelogram.

DC resistivity was measured between the room temperature and 10 K by the standard four-contact technique.

The dielectric function of $\beta'$-EtMe$_3$Sb in the frequency range 40 Hz–10 MHz was extracted from the complex conductance measured in the temperature sweeps between 300 K and 4.2 K by Agilent 4294A, HP4284A, and Keysight E4980AL-102 precision impedance analyzers, and the spectra were extracted from the frequency-sweeps at fixed temperatures. The employed ac signal level was 50 mV, verified to be well within the linear response regime. Best contacts for transport and dielectric measurements are produced by carbon paint applied directly to the sample surface. Extrinsic effects, especially those due to contact resistance and surface layer capacitance, were ruled out with scrutiny [37].

The out-of-plane ($\mathbf{E} \parallel c$) and in-plane ($\mathbf{E} \parallel a$ and $\mathbf{E} \parallel b$) vibrational spectroscopy measurements down to 5 K were conducted by an IR microscope attached to a Bruker Vertex 80v Fourier-transform spectrometer with 1cm$^{-1}$ resolution.

## APPENDIX B: STRUCTURE

The experimental structure was obtained by x-ray diffraction measurements [19,20]. We have used Mercury software for visualization and analysis of crystal structures [38] and Platon software for additional symmetry space group verification [39]. The $\beta'$-EtMe$_3$Sb crystal has a layered structure along the $c$ axis with global symmetry space group $C2/c$ (Fig. 7). There are two equivalent anion layers consisting of four molecular dimers (two in the central and two in the side layers), where dimers stack face-to-face along two diagonal directions [110]
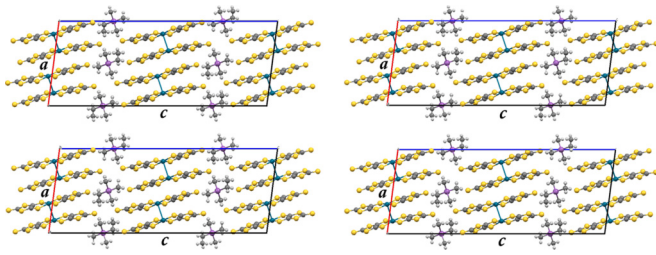
FIG. 9. Four relaxed configurations of $\beta'$-EtMe$_3$Sb, higher in energy by 45–79 meV from the ground state, in the $ac$ plane projected along the $b$ axis. In two configurations displayed in the left column, two ends of each dimer are in the same environment, but the environment differs within the layer, as well as between the center and side layers. In two configurations displayed in the right column, two ends of each dimer are in different environment. The environment differs within the layer, but is the same in the center and side layers. Yellow, grey, light grey, and violet circles denote sulfur, carbon, hydrogen, and antimony atoms, respectively. The unit cell is marked as a parallelogram.

and [1$\bar{1}$0]. There are four cations; each cation consists of three methyl CH$_3$ groups (denoted Me) and one Ethyl CH$_2$-CH$_3$ group (denoted Et) which can occupy one of two different equally probable orientations. The latter indicates that the formation of several crystallographic configurations is possible (Figs. 8, 9, 10, and 11).

Relaxed ground state structure of $\beta'$-EtMe$_3$Sb in the $ac$ plane projected along the $b$ axis as obtained from vdW-DF calculations is shown in Fig. 1(b) and in upper panel of Fig. 8. In this configuration, the Et and the Me sites are in
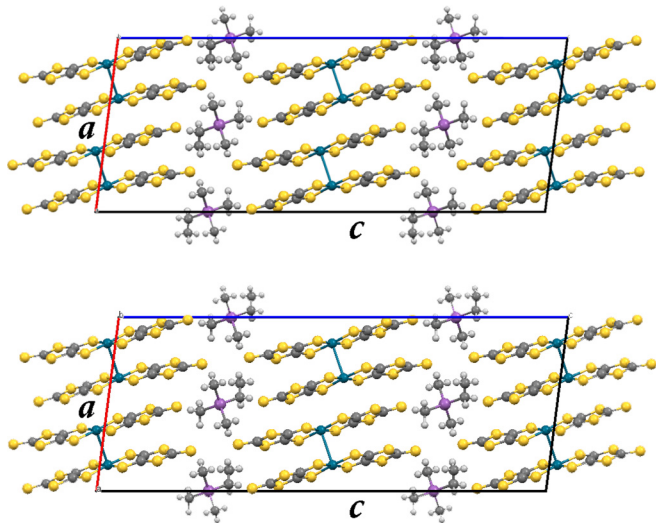


FIG. 10. Two relaxed configurations of $\beta'$-EtMe$_3$Sb, at 146 meV above the ground state, in the $ac$ plane projected along the $b$ axis. In both configurations, two ends of each dimer are in different environments: one end is near Et, while the other end is near the Me group. The environment of dimer ends is the same in the center and side layers. However, note, that in contrast to the configurations in Figs. 8 and 9, 50%–50% occupancy of the two Et sites of the original average structure is not preserved. Yellow, grey, light grey, and violet circles denote sulfur, carbon, hydrogen, and antimony atoms, respectively. The unit cell is marked as a parallelogram.
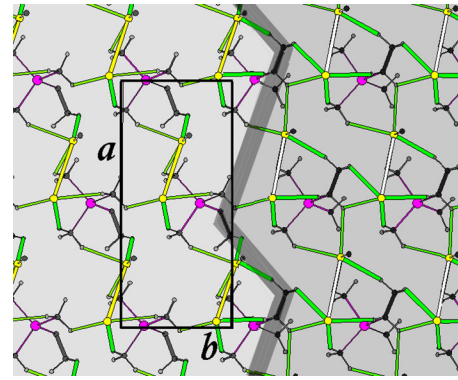


FIG. 11. View of the layers of cations connected to the end sulfur atoms of the [Pd(dmit)$_2$]$_2$ dimers in the $ab$ plane projected along the $c$ axis. For simplicity, only one layer of cations with terminal S atoms in one neighboring anion layer is shown. The unit cell is marked as a rectangle. Gray thick line denotes the phase boundary. Yellow, grey, light grey, and violet circles denote sulfur, carbon, hydrogen, and antimony atoms, respectively. Yellow and white full lines denote small and large S-S dimer openings in the vicinity of Me and Et cation groups, respectively. Thick full line stands for the carbon-carbon bond within the Et group. Assumed local inversion symmetry breaking promotes formation of an antiphase boundary between two neighboring domains, in which overall 50%–50% occupancy of the two Et sites in the original average structure is preserved.

the proximity of terminal sulfur atoms of DMIT molecular dimers in the central and side layer, respectively. Hydrogen bonds (shorter than the sum of the vdW radii) between the terminal sulfur atoms of the [Pd(dmit)$_2$]$_2$ dimers and Et and Me groups of the cations are indicated by green and blue full lines, respectively. Thick and thin lines denote bonds of 2.7–2.8 Å and 2.8–2.9 Å, respectively. There are eight short contacts between two terminal S atoms at one end of dimer and Et groups of cations, while there are only six contacts to Me groups. The opening between two terminal S atoms at the end of dimer is larger near Et (3.910 Å) than near to the Me (3.645 Å) group.

## APPENDIX C: NUMERICAL CALCULATIONS AND STRUCTURAL PARAMETERS

To compute the electronic structure of $\beta'$-EtMe$_3$Sb, we have employed the self-consistently implemented van der Waals density functional (vdW-DF) [21–23] for correlation with optB88 for exchange [24]. The expansion in the plane waves was done with a cutoff energy of 700 eV, the Brillouin zone was sampled by $1 \times 2 \times 2$ Monkhorst-Pack choice of $k$ points [41]. For the atomic coordinates of $\beta'$-EtMe$_3$Sb, the experimental structure obtained by x-ray diffraction measurements at room temperature was used and adopted to construct eight possible structural configurations arising from two equally probable orientations of Et subgroups of EtMe$_3$Sb cations (see Figs. 8, 9, and 10 for possible configurations). We relaxed the structure, allowing for change of the volume and the shape of the unit cell together with atomic positions within, till the forces on atoms dropped below 1 meV/Å. Originally the unit cell contained two dimers per layer as indicated by the x-ray data. However,

TABLE I. Unit cell parameters of $\beta'$-EtMe$_3$Sb obtained by x-ray diffraction measurements (left column), *ab initio* calculations based on PBE functional (central column), and on vdW-DF (right column).

| Unit cell parameters | Exp | Calc: PBE | Calc: vdW-DF |
|---|---|---|---|
| $a$ | 14.503000 Å | 15.9149 Å | 14.2688 Å |
| $b$ | 6.398900 Å | 6.91156 Å | 6.29494 Å |
| $c$ | 37.243999 Å | 37.7632 Å | 37.0734 Å |
| $\alpha$ | 90.000000° | 90.3248° | 90.5347° |
| $\beta$ | 97.351997° | 95.5322° | 97.7111° |
| $\gamma$ | 90.000000° | 89.6834° | 89.3776° |
| $V$ | 3427.96 Å$^3$ | 4170.00 Å$^3$ | 3299.57 Å$^3$ |
| $a$(Calc)-$a$(Exp)/$a$(Exp) | | +9.7% | −1.6% |
| $b$(Calc)-$b$(Exp)/$b$(Exp) | | +8.0% | −1.6% |
| $c$(Calc)-$c$(Exp)/$c$(Exp) | | +1.4% | −0.5% |
| $V$(Calc)-$V$(Exp)/$V$(Exp) | | +21.6% | −3.7% |

after the full relaxation, the unit cell, due to symmetry, can be reduced to the one with only one dimer per layer. Importantly, relaxation without the van der Waals functional yielded the structure very different from the experimental one (see Table I), showing that the standard semilocal density functionals may lead to erroneous predictions for the structure that is partially vdW bonded.

More details on the band structure are shown in Figs. 12 and 13.

Electronic charge redistribution induced by the cation-anion interaction in the relaxed ground state was calculated as the difference between the charge density of the complete system and its constituents, i.e., cations and anions. Two isosurfaces for +0.01 $e$/Å$^3$ and −0.01 $e$/Å$^3$ are shown in Fig. 2: electron accumulation (red) and depletion (blue). The averaged charge density in the $ac$ plane is obtained by the following procedure: we introduce cuts along the $ac$ planes, each cut showing a charge redistribution density, and then take the average over all these planes. The red-tinted and blue-tinted regions in the figure correspond to electron accumulation and depletion, respectively. Green color shows negligible charge redistribution density.
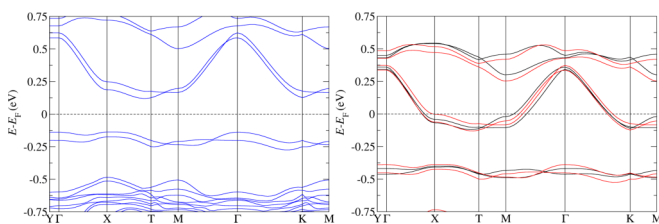


FIG. 12. Band structure of the relaxed ground state of $\beta'$-EtMe$_3$Sb plotted along the high-symmetry directions. Left panel: If only the molecular self-standing subsystem is calculated, the generic anion bands (blue lines) are obtained. These bands exhibit a gap which exceeds those calculated for $\kappa$-CuCN and $\kappa$-AgCN [7,8]. Right panel: Shifting the generic anion bands by 250 meV (red lines) results in a fair coincidence with the band structure calculated for the complete system (black), thereby revealing the dominantly anion-derived band character around the Fermi energy.
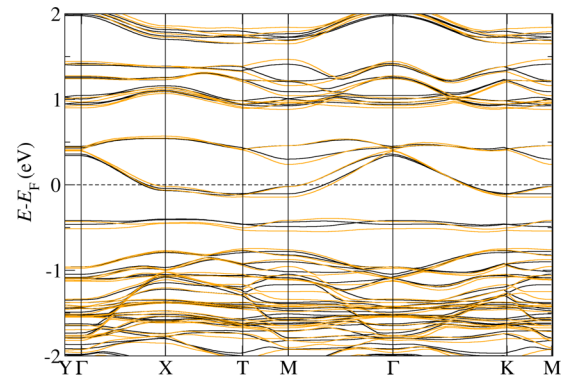


FIG. 13. Band structure of $\beta'$-EtMe$_3$Sb at ambient pressure (black) and at $p = 11$ kbar (orange) plotted along the high-symmetry points. The band structure remains almost unchanged under pressure although the volume is reduced by 5%. This indicates that the structure is dominantly stabilized by van der Waals forces.
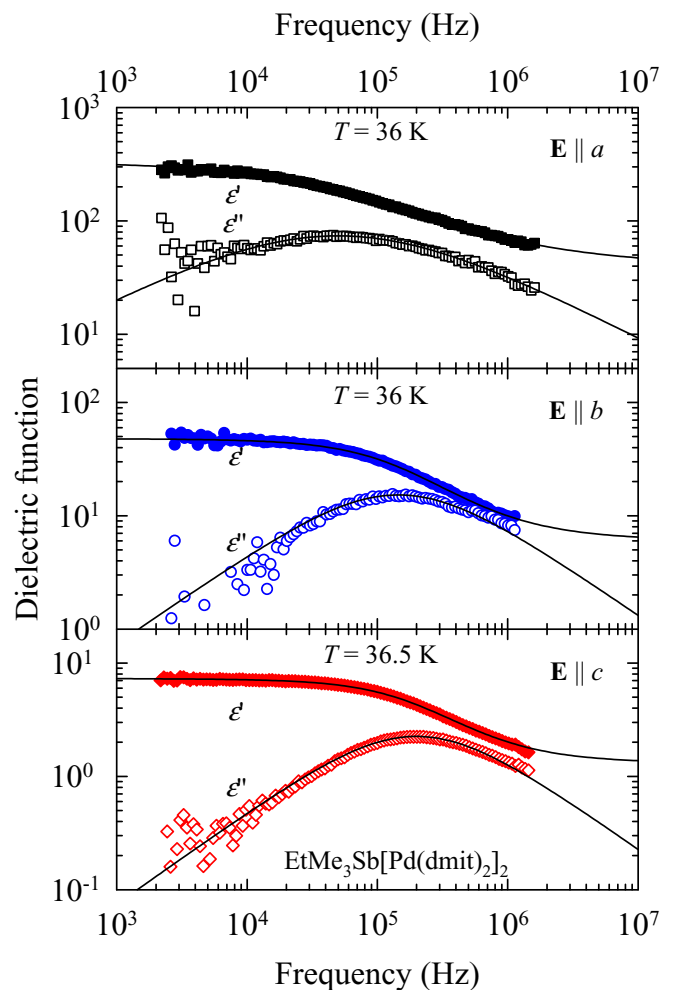


FIG. 14. Double logarithmic plot of the frequency dependence of the real ($\varepsilon'$) and imaginary ($\varepsilon''$) parts of the dielectric function in representative single crystals of $\beta'$-EtMe$_3$Sb at $T = 36$ K. Data for $\mathbf{E} \parallel a$, for $\mathbf{E} \parallel b$, and for $\mathbf{E} \parallel c$ are shown in upper, center, and lower panels, respectively. The full lines are fits to a generalized Debye function (see text).

## APPENDIX D: DC AND LOW-FREQUENCY CHARGE RESPONSE

In Fig. 14, we show representative spectra of the real and imaginary parts of the dielectric function $\varepsilon(\omega, T) = \varepsilon'(\omega, T) - i\varepsilon''(\omega, T)$ of $\beta'$-EtMe$_3$Sb recorded at $T = 36$ K for the directions $\mathbf{E} \parallel a$, $\mathbf{E} \parallel b$, and $\mathbf{E} \parallel c$. These spectra bear features commonly found in relaxation-type dielectric response. A low-frequency constant plateau is followed by a decrease of $\varepsilon'$ with increasing frequency. Associated with this drop is a Kramers-Kronig-consistent peak in $\varepsilon''$, which gives it a characteristic bell-like shape. The main features of this relaxation are well described by the generalized Debye expression $\varepsilon(\omega) - \varepsilon_{HF} = \Delta\varepsilon / [1 + (i\omega\tau_0)^{1-\alpha}]$ where $\Delta\varepsilon = \varepsilon_0 - \varepsilon_{HF}$ corresponds to the strength of the mode, $\varepsilon_0$ and $\varepsilon_{HF}$ are the static and high-frequency dielectric constant, respectively, $\tau_0$ is the mean relaxation time, and $1 - \alpha$ describes the symmetric broadening of the relaxation time distribution.

Data shown in Fig. 15 demonstrate the behavior according to Barton-Nakajima-Namikawa (BNN) formula $\sigma(0) = \epsilon_0 \Delta\varepsilon \omega_0$, a feature common to disordered systems [40]. $\sigma(0)$ and $\omega_0$ stand for dc conductivity and $1/\tau_0$, respectively. This behavior is found not only in the direction perpendicular to the molecular dimer planes, as previously shown in Ref. [5], but also within molecular dimer planes.
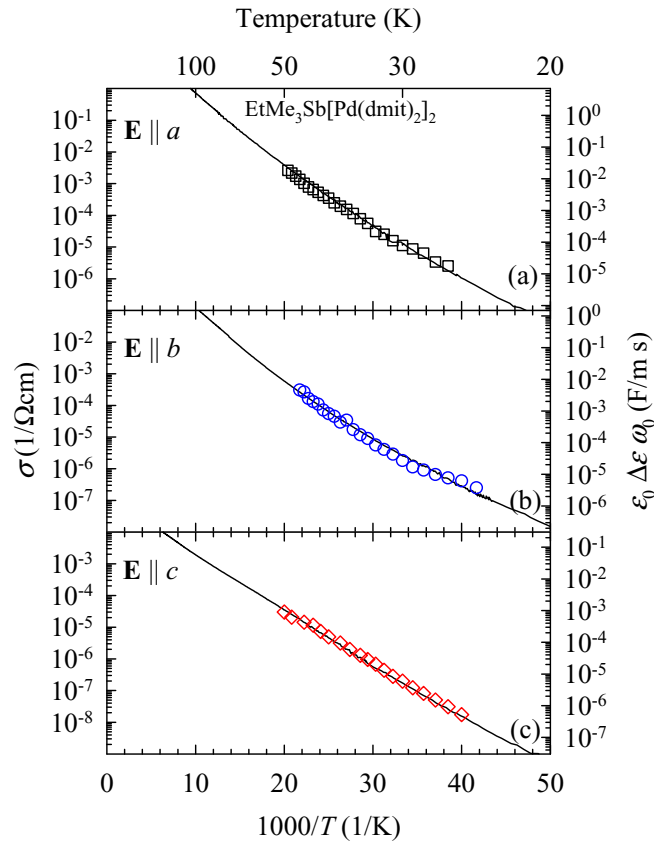


FIG. 15. DC conductivity, $\sigma$ (full line) and the product $\epsilon_0 \Delta\varepsilon \omega_0$ of $\epsilon_0$, dielectric strength $\Delta\varepsilon$, and inverse of the mean relaxation time $1/\tau_0$ (full circles) of $\beta'$-EtMe$_3$Sb versus inverse temperature. Data for the measurements with the applied ac field $\mathbf{E} \parallel a$, $\mathbf{E} \parallel b$, and $\mathbf{E} \parallel c$ are shown by black squares, blue circles, and red diamonds, respectively.

## APPENDIX E: IN-PLANE RESPONSE OF CHARGE-SENSITIVE VIBRATION

In addition to the out-of-plane investigations shown in the main paper, for the sake of completeness, here we present the results of optical measurements parallel to the conducting planes for $\mathbf{E} \parallel a$ and $\mathbf{E} \parallel b$. Figure 16 shows the corresponding spectra (left panels) as well as the comparison of Fano fit parameters including the $\mathbf{E} \parallel c$ data (right panels). None of the modes splits upon cooling, confirming our general conclusion that there is no sizable charge disproportionation.

The intramolecular $\nu_2$ mode implies an oscillating dipole moment along the molecular axis. Thus the $\mathbf{E} \parallel c$ geometry is most suitable to probe molecular charge through the $\nu_2$ vibration, as discussed in the main manuscript. The weak shoulder at 1323 cm$^{-1}$ (Fig. 6), most apparent at low temperatures, is also observed in the normal (non-charge-ordered) state of $\beta'$-Et$_2$Me$_2$Sb[Pd(dmit)$_2$]$_2$ [35]. Since, for the in-plane measurement, the electric field is polarized almost perpendicular to the molecules, the coupling to the $\nu_2$ mode is very weak. The large electronic background within the conducting layer enables strong electron-molecular vibrational (emv) coupling among these molecular vibrations that make the dimeric $\nu_2$ vibrations susceptible for an in-plane electric field. For that reason, we can identify the mode for both $\mathbf{E} \parallel a$ and $\mathbf{E} \parallel b$ (see Fig. 16). It should be noted, however, that the emv coupling crucial for the in-plane features is strongly affected by the electronic background while the out-of-plane response probes the pure infrared-active vibration. At high temperatures,
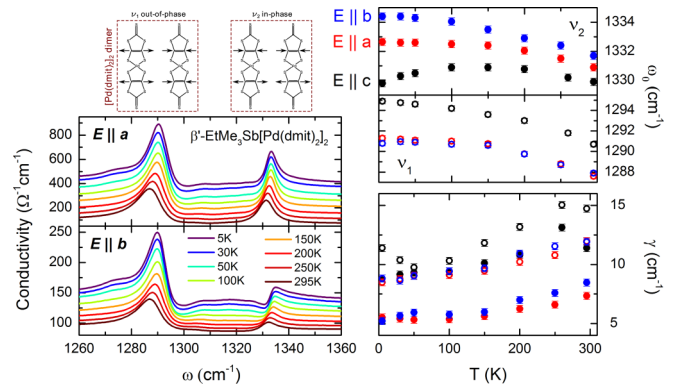


FIG. 16. Polarization-dependent temperature evolution of the in-plane optical conductivity ($\mathbf{E} \parallel a$, $\mathbf{E} \parallel b$) of $\beta'$-EtMe$_3$Sb in the range of the out-of-phase combination of the $\nu_1$ vibration and in-phase combination of the $\nu_2$ mode in a [Pd(dmit)$_2$]$_2$ dimer. Apart from the smaller intensity and more pronounced asymmetry along the crystallographic $b$-direction, the resonance frequency and temperature dependence of the in-plane modes are similar. In general, there is a typical blue-shift upon cooling down from the incoherent, highly conducting regime. When entering the Mott insulating regime, i.e., upon crossing the quantum Widom line at 120 K [4], the shift comes to a halt. This behavior is distinct from the out-of-plane response ($\mathbf{E} \parallel c$), where the $\nu_2$ mode shows an unusual red shift at low temperatures. The differences between in- and out-of-plane response stem from the influence of the electronic background; for $\mathbf{E} \parallel c$ we probe the $\nu_2$ vibration undisturbed by the electronic background, so it provides a clean probe of the molecular charge. Except the 295 K data, all curves are shifted vertically by a constant value.
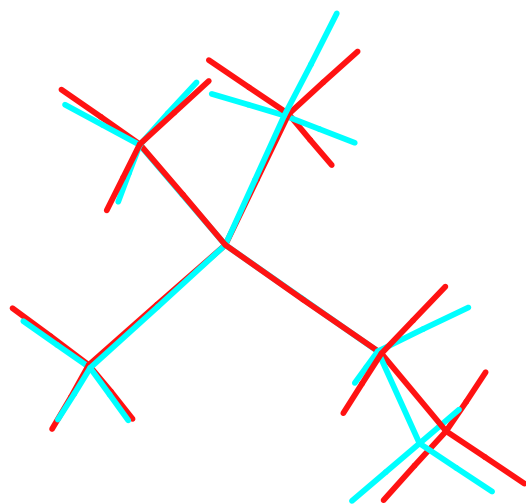
FIG. 17. The overlap of the $Sb(CH_3)_3(CH_2CH_3)^+$ in the gas phase (red) and in a crystal (blue).



FIG. 18. Potential energy curve (in eV) for the methyl rotation in the solid state $\beta'$-EtMe$_3$Sb[Pd(dmit)$_2$]$_2$ as computed using vdW-DF with optB88. The energies of the ground (red) and first excited (green) vibrational states are shown.

above 150 K, both inspected vibrations show a blue shift, which is typical of phonon hardening due to lattice contraction upon cooling. Interestingly, while the emv coupled mode exhibits a weaker temperature dependence below 150 K, the intramolecular $\nu_2$ vibrations probed by $\mathbf{E} \parallel c$ shifts toward lower frequencies. These changes in resonance frequencies appear in a similar temperature range as the freezing of cationic motion.

Now we focus on the symmetric $\nu_1$ mode, which should be Raman- and not infrared-active for the vibration of the single molecule. Coupling to the electronic background causes the out-of-phase dimeric motion to appear in the optical spectra. Since this coupling is weak perpendicular to the stacks, its intensity is smaller than that of the infrared-active $\nu_2$ vibration for $\mathbf{E} \parallel c$. In presence of the strong conductivity of the Mott-Hubbard band for in-plane polarization, however, it becomes significantly stronger than the dimeric $\nu_2$ mode. Overall, the temperature dependence of the $\nu_1$ mode is similar as for the in-plane $\nu_2$ vibration, reflecting the influence of the electronic background.

### APPENDIX F: NUMERICAL CALCULATIONS OF CATION MOTION

Calculations of isolateted $Sb(CH_3)_3(CH_2CH_3)^+$ were performed using DFT with the long-range corrected wB97XD functional with dispersion corrections [42,43] and the 6-311+G(d,p) basis set. The effective core potentials for the antimony atom [44–46] was used as part of the LanL2DZdp basis set [47,48]. All electronic structure calculations on the isolated system were performed with the Gaussian09 suite of programs [49] with the pruned (99590) grid ("ultrafine" grid) and the tight option for geometry optimization. The potential energ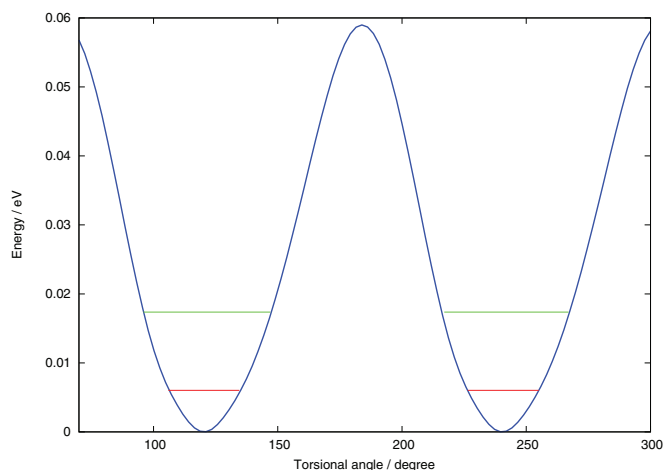y surfaces for $CH_3$ rotation were computed for the crystal structure and the rotational energy levels were calculated on the 1D potential energy surfaces using the Grid Hamiltonian Method [50,51].

Figure 17 shows the overlap of the $Sb(CH_3)_3(CH_2CH_3)^+$ in the gas phase and in a crystal. In the gas phase, the $CH_3$-Sb-$CH_3$ angles are equal to $107.6°$, $108.7°$, and $111.9°$, and deviate from the respective values in the crystal by $0.5°$. A somewhat larger deviation is found in the bond distances. In the isolated system, the three Sb-$CH_3$ bonds are nearly identical and equal to 2.131 Å whereas the Sb-Et bond is longer and equal to 2.151 Å. The bonds are shorter in the crystal structure and amount to 2.095 Å and 2.107 Å, respectively. The most significant deviation, however, is found in the C-C bond. The crystal structure is characterized by a C-C bond of 1.268 Å whereas in the gas phase the bond is elongated to 1.535 Å. At the $Sb(CH_3)_3(CH_2CH_3)^+$ minimum, we performed a normal mode analysis showing delocalization of low frequency modes. The lowest frequency motion at 42.8 cm$^{-1}$ corresponds predominantly to the libration of ethyl group, whereas four normal modes in the range between 96.5 and 114.9 cm$^{-1}$ are localized on methyl groups.

The potential energy profile for methyl rotation of $Sb(CH_3)_3(CH_2CH_3)^+$ in the solid state $\beta'$-EtMe$_3$Sb as computed using vdw-DF with optB88 is shown in Fig. 18. The orientation of $CH_3$ group was varied in the interval $0° < \theta < 90°$ in the steps of $10°$ while the remaining degrees of freedom were kept fixed at the crystal structure values. The barrier to $CH_3$ rotation is 0.059 eV and the ground-state rotational tunneling splitting is 0.093 $\mu$eV. The first excited vibrational state is found at 0.011 eV or 91.4 cm$^{-1}$ higher in energy, hence confirming the gas phase results.

[1] W. P. Anderson, Mat. Res. Bull. **8**, 153 (1973).

[2] L. Balents, Nature **464**, 199 (2010).

[3] L. Savary and L. Balents, Rep. Prog. Phys. **80**, 016502 (2017); Y. Zhou, K. Kanoda, and T-K. Ng, Rev. Mod. Phys. **89**, 025003 (2017).

[4] A. Pustogow, M. Bories, A. Löhle, R. Rösslhuber, E. Zhukova, B. Gorshunov, S. Tomić, J. A. Schlueter, R. Hübner, T. Hiramatsu, Y. Yoshida, G. Saito, R. Kato, T.-H. Lee, V. Dobrosavljević, S. Fratini, and M. Dressel, arXiv:1710.07241.

[5] M. Abdel-Jawad, I. Terasaki, T. Sasaki, N. Yoneyama, N. Kobayashi, Y. Uesu, and C. Hotta, Phys. Rev. B **82**, 125119 (2010); M. Abdel-Jawad, N. Tajima, R. Kato, and I. Terasaki, *ibid.* **88**, 075139 (2013).

[6] K. Itoh, H. Itoh, M. Naka, S. Saito, I. Hosako, N. Yoneyama, S. Ishihara, T. Sasaki, and S. Iwai, Phys. Rev. Lett. **110**, 106401 (2013).

[7] M. Pinterić, M. Čulo, O. Milat, M. Basletić, B. Korin-Hamzić, E. Tafra, A. Hamzić, T. Ivek, T. Peterseim, K. Miyagawa, K. Kanoda, J. A. Schlueter, M. Dressel, and S. Tomić, Phys. Rev. B **90**, 195139 (2014); M. Dressel, P. Lazić, A. Pustogow, E. Zhukova, B. Gorshunov, J. A. Schlueter, O. Milat, B. Gumhalter, and S. Tomić, *ibid.* **93**, 081201(R) (2016).

[8] M. Pinterić, P. Lazić, A. Pustogow, T. Ivek, M. Kuveždić, O. Milat, B. Gumhalter, M. Basletić, M. Čulo, B. Korin-Hamzić, A. Löhle, R. Hübner, M. Sanz Alonso, T. Hiramatsu, Y. Yoshida, G. Saito, M. Dressel, and S. Tomić, Phys. Rev. B **94**, 161105(R) (2016).

[9] Y. Shimizu, K. Miyagawa, K. Kanoda, M. Maesato, and G. Saito, Phys. Rev. Lett. **91**, 107001 (2003); Y. Kurosaki, Y. Shimizu, K. Miyagawa, K. Kanoda, and G. Saito, *ibid.* **95**, 177001 (2005); Y. Shimizu, K. Miyagawa, K. Kanoda, M. Maesato, and G. Saito, Phys. Rev. B **73**, 140407 (2006); T. Isono, T. Terashima, K. Miyagawa, K. Kanoda, and S. Uji, Nat. Commun. **7**, 13494 (2016).

[10] Y. Shimizu, T. Hiramatsu, M. Maesato, A. Otsuka, H. Yamochi, A. Ono, M. Itoh, M. Yoshida, M. Takigawa, Y. Yoshida, and G. Saito, Phys. Rev. Lett. **117**, 107203 (2016).

[11] T. Itou, A. Oyamada, S. Maegawa, M. Tamura, and R. Kato, Phys. Rev. B **77**, 104413 (2008); T. Itou, A. Oyamada, S. Maegawa, and R. Kato, Nat. Phys. **6**, 673 (2010); T. Itou, K. Yamashita, M. Nishiyama, A. Oyamada, S. Maegawa, K. Kubo, and R. Kato, Phys. Rev. B **84**, 094405 (2011); D. Watanabe, M. Yamashita, S. Tonegawa, Y. Oshima, H. M. Yamamoto, R. Kato, I. Sheikin, K. Behnia, T. Terashima, S. Uji, T. Shibauchi, and Y. Matsuda, Nat. Commun. **3**, 1090 (2012).

[12] D. A. Huse and V. Elser, Phys. Rev. Lett. **60**, 2531 (1988).

[13] C. Hotta, Phys. Rev. B **82**, 241104 (2010); Crystals **2**, 1155 (2012).

[14] M. Naka and S. Ishihara, J. Phys. Soc. Jpn. **82**, 023701 (2013); Phys. Rev. B **93**, 195114 (2016).

[15] H. Li, R. T. Clay, and S. Mazumdar, J. Phys.: Condens. Matter **22**, 272201 (2010); S. Dayal, R. T. Clay, H. Li, and S. Mazumdar, Phys. Rev. B **83**, 245106 (2011).

[16] H. Gomi, M. Ikenaga, Y. Hiragi, D. Segawa, A. Takahashi, T. J. Inagaki, and M. Aihara, Phys. Rev. B **87**, 195126 (2013); H. Gomi, T. J. Inagaki, and A. Takahashi, *ibid.* **93**, 035105 (2016).

[17] K. Sedlmeier, S. Elsässer, D. Neubauer, R. Beyer, D. Wu, T. Ivek, S. Tomić, J. A. Schlueter, and M. Dressel, Phys. Rev. B **86**, 245103 (2012).

[18] T. Furukawa, K. Miyagawa, T. Itou, M. Ito, H. Taniguchi, M. Saito, S. Iguchi, T. Sasaki, and K. Kanoda, Phys. Rev. Lett. **115**, 077001 (2015).

[19] R. Kato, T. Fukunaga, H. M. Yamamoto, K. Ueda, and C. Hengbo, Phys. Status Solidi B **249**, 999 (2012).

[20] R. Kato and C. Hengbo, Crystals **2**, 861 (2012), https://www.ccdc.cam.ac.uk/structures.

[21] M. Dion, H. Rydberg, E. Schröder, D. C. Langreth, and B. I. Lundqvist, Phys. Rev. Lett. **92**, 246401 (2004).

[22] G. Román-Pérez and J. M. Soler, Phys. Rev. Lett. **103**, 096102 (2009).

[23] J. Klimeš, D. R. Bowler, and A. Michaelides, Phys. Rev. B **83**, 195131 (2011).

[24] F. Mittendorfer, A. Garhofer, J. Redinger, J. Klimeš, J. Harl, and G. Kresse, Phys. Rev. B **84**, 201401 (2011).

[25] K. Nakamura, Y. Yoshimoto, and M. Imada, Phys. Rev. B **86**, 205117 (2012).

[26] E. P. Scriven and B. J. Powell, Phys. Rev. Lett. **109**, 097206 (2012).

[27] T. Tsumuraya, H. Seo, M. Tsuchiizu, R. Kato, and T. Miyazaki, J. Phys. Soc. Jpn. **82**, 033709 (2013).

[28] A. C. Jacko, L. F. Tocchio, H. O. Jeschke, and R. Valenti, Phys. Rev. B **88**, 155139 (2013).

[29] M. Pinterić, D. Rivas Gongora, Ž. Rapljenović, T. Ivek, M. Čulo, B. Korin-Hamzić, O. Milat, B. Gumhalter, P. Lazić, M. Sanz Alonso, W. Li, A. Pustogow, G. Gorgen Lesseux, M. Dressel and S. Tomić, Crystals **8**, 190 (2018).

[30] Q. Q. Ge, H. C. Xu, X. P. Shen, M. Xia, B. P. Xie, F. Chen, Y. Zhang, R. Kato, T. Tsumuraya, T. Miyazaki, M. Matsunami, S. Kimura, and D. L. Feng, Phys. Rev. B **89**, 075105 (2014).

[31] A. L. Efros and B. I. Shklovskii, J. Phys. C: Solid State Phys. **8**, L49 (1975).

[32] R. H. McKenzie, Comments Cond. Matt. Phys. **18**, 309 (1998).

[33] H. Fukuyama, J. Kishine, and M. Ogata, J. Phys. Soc. Jpn. **86**, 123706 (2017).

[34] T. Itou, E. Watanabe, S. Maegawa, A. Tajima, N. Tajima, K. Kubo, R. Kato, and K. Kanoda, Sci. Adv. **3**, e1601594 (2017).

[35] T. Yamamoto, Y. Nakazawa, M. Tamura, T. Fukunaga, R. Kato, and K. Yakushi, J. Phys. Soc. Jpn. **80**, 074717 (2011).

[36] M. Poirier, M-O. Proulx, and R. Kato, Phys. Rev. B **90**, 045147 (2014).

[37] T. Ivek, B. Korin-Hamzić, O. Milat, S. Tomić, C. Clauss, N. Drichko, D. Schweitzer, and M. Dressel, Phys. Rev. B **83**, 165128 (2011).

[38] C. F. Macrae, P. R. Edgington, P. McCabe, E. Pidcock, G. P. Shields, R. Taylor, M. Towler, and J. van de Streek, J. Appl. Cryst. **39**, 453 (2006).

[39] A. L. Spek, Acta Cryst. D **65**, 148 (2009).

[40] J. C. Dyre and T. B. Schröder, Rev. Mod. Phys. **72**, 873 (2000).

[41] H. J. Monkhorst and J. D. Pack, Phys. Rev. B **13**, 5188 (1976).

[42] J.D. Chai and M. Head-Gordon, J. Chem. Phys. **128**, 084106 (2008).

[43] J.D. Chai and M. Head-Gordon, Phys. Chem. Chem. Phys. **10**, 6615 (2008).

[44] P. J. Hay and W. R. Wadt, J. Chem. Phys. **82**, 270 (1985).

[45] P. J. Hay and W. R. Wadt, J. Chem. Phys. **82**, 284 (1985).

[46] P. J. Hay and W. R. Wadt, J. Chem. Phys. **82**, 299 (1985).

[47] T. H. Dunning and P. J. Hay, in *Methods of Electronic Structure*, Vol. 3 (Plenum Publishing Company, New York, 1977).

[48] C. E. Check, T. O. Faust, J. M. Bailey, B. J. Wright, T. M. Gilbert, and L. S. Sunderlin, J. Phys. Chem. A **105**, 8111 (2001).

[49] M. J. Frisch, G. W. Trucks, H. B. Schlegel, G. E. Scuseria, M. A. Robb, J. R. Cheeseman, G. Scalmani, V. Barone, B. Mennucci, G. A. Petersson, H. Nakatsuji, M. Caricato, X. Li, H. P. Hratchian, A. F. Izmaylov, J. Bloino, G. Zheng, J. L. Sonnenberg, M. Hada, M. Ehara, K. Toyota, R. Fukuda, J. Hasegawa, M. Ishida, T. Nakajima, Y. Honda, O. Kitao, H. Nakai, T. Vreven, J. A. Montgomery, Jr., J. E. Peralta, F. Ogliaro,

M. Bearpark, J. J. Heyd, E. Brothers, K. N. Kudin, V. N. Staroverov, R. Kobayashi, J. Normand, K. Raghavachari, A. Rendell, J. C. Burant, S. S. Iyengar, J. Tomasi, M. Cossi, N. Rega, J. M. Millam, M. Klene, J. E. Knox, J. B. Cross, V. Bakken, C. Adamo, J. Jaramillo, R. Gomperts, R. E. Stratmann, O. Yazyev, A. J. Austin, R. Cammi, C. Pomelli, J. W. Ochterski, R. L. Martin, K. Morokuma, V. G. Zakrzewski, G. A. Voth, P. Salvador, J. J. Dannenberg, S. Dapprich, A. D. Daniels, Farkas, J. B. Foresman, J. V. Ortiz, J. Cioslowski, and D. J. Fox, *Gaussian 09 Revision A.1* (Gaussian Inc., Wallingford, CT, 2009).

[50] C. C. Marston and G. G. Balint-Kurti, J. Chem. Phys. **91**, 3571 (1989).

[51] I. Matanović and N. Došlić, J. Phys. Chem. A **109**, 4185 (2005).